Structure of ATP synthase from *Paracoccus denitrificans* determined by X-ray crystallography at 4.0 Å resolution

Edgar Morales-Rios[a], Martin G. Montgomery[a], Andrew G. W. Leslie[b,1], and John E. Walker[a,1]

[a]Medical Research Council Mitochondrial Biology Unit, Cambridge Biomedical Campus, Cambridge CB2 0XY, United Kingdom; and [b]Medical Research Council Laboratory of Molecular Biology, Cambridge Biomedical Campus, Cambridge CB2 0QH, United Kingdom

Contributed by John E. Walker, September 4, 2015 (sent for review July 28, 2015; reviewed by Stanley D. Dunn, Robert H. Fillingame, and Dale Wigley)

The structure of the intact ATP synthase from the α-proteobacterium *Paracoccus denitrificans*, inhibited by its natural regulatory ζ-protein, has been solved by X-ray crystallography at 4.0 Å resolution. The ζ-protein is bound via its N-terminal α-helix in a catalytic interface in the F_1 domain. The bacterial F_1 domain is attached to the membrane domain by peripheral and central stalks. The δ-subunit component of the peripheral stalk binds to the N-terminal regions of two α-subunits. The stalk extends via two parallel long α-helices, one in each of the related b and b′ subunits, down a noncatalytic interface of the F_1 domain and interacts in an unspecified way with the a-subunit in the membrane domain. The a-subunit lies close to a ring of 12 c-subunits attached to the central stalk in the F_1 domain, and, together, the central stalk and c-ring form the enzyme's rotor. Rotation is driven by the transmembrane proton-motive force, by a mechanism where protons pass through the interface between the a-subunit and c-ring via two half-channels in the a-subunit. These half-channels are probably located in a bundle of four α-helices in the a-subunit that are tilted at ∼30° to the plane of the membrane. Conserved polar residues in the two α-helices closest to the c-ring probably line the proton inlet path to an essential carboxyl group in the c-subunit in the proton uptake site and a proton exit path from the proton release site. The structure has provided deep insights into the workings of this extraordinary molecular machine.

Paracoccus denitrificans | ATP synthase | structure | regulation | proton translocation

The ATP synthases (F-ATPases) found in eubacteria, chloroplasts, and mitochondria are multiprotein molecular machines with a rotary action that provide most cellular ATP. Our understanding of how they work has come mainly from single-molecule studies of rotation made almost entirely on bacterial F-ATPases (1) and from structures of their constituent domains determined predominantly with enzymes from mitochondria (2–5). The most complete high-resolution structure contains about 85% of the bovine F-ATPase, built up from substructures determined by X-ray crystallography (2), within the constraints of an overall structure determined by cryo-EM (6). This model provides many details about the catalytic mechanism of the F_1 domain (2, 5); its mode of inhibition by the natural inhibitor protein of F_1-ATPase, IF_1 (2, 4); and the design of the rotor, an ensemble of a membrane-bound ring of eight c-subunits, and the elongated central stalk, which penetrates into the catalytic F_1 domain. However, it lacks a crucial region that would help to explain how the enzyme uses the transmembrane proton-motive force produced by respiration or photosynthesis to generate the turning of the rotor in its membrane domain and other features that keep the proton-motive force coupled to the synthesis of ATP.

Few structural studies have been carried out on the F-ATPases from eubacteria. Their subunit compositions are simpler than the subunit compositions of mitochondrial enzymes (7–9). They contain the same or analogous eight or nine core subunits that constitute the catalytic domain, rotor, and stator, but they lack the six or more supernumerary membrane subunits of the mitochondrial enzyme that have no known role in catalysis (2). Structures have been described of the F_1 domains of the enzymes from *Escherichia coli* (10, 11), *Caldalkalibacillus thermarum* (12), and *Geobacillus stearothermophilus* (formerly *Bacillus* PS3) (13); of the $\alpha_3\beta_3$-subcomplex of the F_1 domain from *G. stearothermophilus* (14); and of isolated c-rings from the rotors of several species (15–19). There is also structural information on the peripheral stalk region of the F-ATPase from *E. coli* and on the N-terminal domain of the δ-subunit and its interaction with the N-terminal region of the α-subunit (20) and segments of the b-subunit (21–23).

Many attempts have been made to crystallize intact F-ATPases, as a prelude to structural analysis, without success until the recent crystallization of the F-ATPase from *Paracoccus denitrificans* (24). This enzyme can only synthesize ATP, and inhibition of hydrolysis involves the ζ-inhibitor protein, found only in α-proteobacteria. As described here, the structure of the inhibited complex has been determined at 4.0 Å resolution. It reveals new features about the mechanism of inhibition by the ζ-protein and about the coupling of the proton-motive force to the synthesis of ATP.

Results and Discussion

Structure Determination. The structure of the *P. denitrificans* F-ATPase–ζ-inhibitor complex was determined by molecular replacement at 4.0 Å resolution. The asymmetrical unit of the crystals

Significance

ATP, the fuel of life, is produced in living cells by a complex molecular machine consisting of two motors linked by a rotor. One motor generates rotation by consuming energy derived from oxidative metabolism or photosynthesis; the other uses energy transmitted by the rotor to put ATP molecules together from their building blocks, ADP and phosphate. One such intact machine from the α-proteobacterium *Paracoccus denitrificans* has been induced to form crystals, providing the means of deducing a blueprint of the machine, giving details of how its components are organized, and providing insights into how it works. The mechanistic principles deduced from the bacterial machine apply to similar molecular machines found in all living organisms.

Author contributions: J.E.W. designed research; E.M.-R. and M.G.M. performed research; E.M.-R., M.G.M., A.G.W.L., and J.E.W. analyzed data; E.M.-R., M.G.M., A.G.W.L., and J.E.W. wrote the paper; and J.E.W. supervised the project.

Reviewers: S.D.D., University of Western Ontario; R.H.F., University of Wisconsin; and D.W., Imperial College, London.

The authors declare no conflict of interest.

Freely available online through the PNAS open access option.

Data deposition: The atomic coordinates have been deposited in the Protein Data Bank, www.pdb.org (PDB ID code 5DN6).

[1]To whom correspondence may be addressed. Email: walker@mrc-mbu.cam.ac.uk or andrew@mrc-lmb.cam.ac.uk.

This article contains supporting information online at www.pnas.org/lookup/suppl/doi:10.1073/pnas.1517542112/-/DCSupplemental.

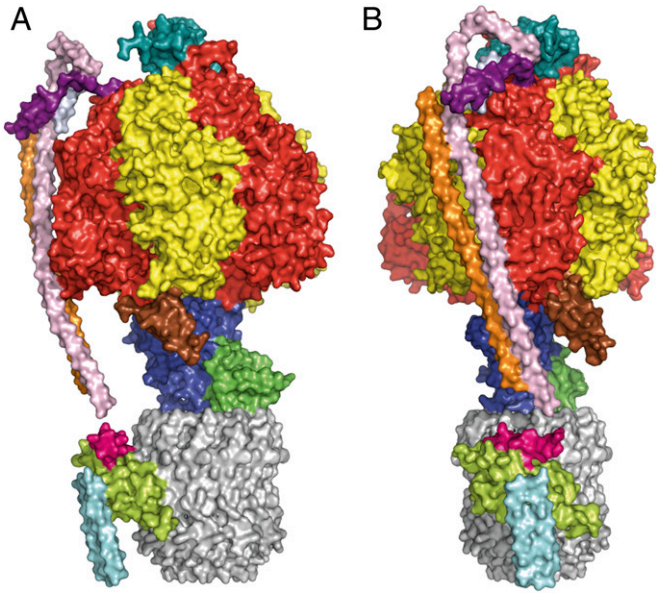

Fig. 1. Structure of the complex of the F-ATPase from *P. denitrificans* with the bound ζ-inhibitor protein. (*A* and *B*) Side views of the enzyme–inhibitor complex in surface representation. *B* is rotated right by 90° relative to *A*. (*Upper*) Membrane extrinsic F_1 catalytic domain (red, yellow, blue, and green corresponding to three α-subunits, three β-subunits, and single γ- and ε-subunits, respectively). In the peripheral stalk, the δ-subunit (top) is sky blue and the long and approximately parallel α-helical segments in orange and pink (chains V and W) extending down the surface of the interface between the α- and β-subunits are parts of the b- and b′-subunits (undistinguished). Unassigned α-helical segments (chains 1 and 2) in the vicinity of the junction between the δ-subunit and b- and b′-subunits are purple and light gray, respectively. Helix-1 of the ζ-inhibitor is brown. (*Lower*) In the membrane domain, the ring of 12 c-subunits is gray and a bundle of four resolved α-helices assigned to the a-subunit is lemon green. An unassigned α-helical segment in magenta (chain 3) lies approximately parallel to α-helices in subunit a, and two unassigned side-by-side transmembrane α-helices (chain Y) are colored light blue.

contains one inhibited complex. The data processing and refinement statistics are summarized in Table S1. The final model (Fig. 1) contains the following residues (where E, TP, and DP denote the subunits comprising the empty, diphosphate-containing, and triphosphate-containing catalytic interfaces, respectively): α_E, 2–190 and 196–511; α_{TP}, 7–193, 198–405, and 411–511; α_{DP}, 28–511; β_E, 3–468; β_{TP}, 4–469; β_{DP}, 2–471; γ, 3–62, 64–73, 78–110, 115–143, 147–166, 170–199, and 212–289; δ, 5–114; ε, 9–83; subunit a, 35 residues in aH3 and aH4 modeled as poly-Ala (residues 1,001–1,035), aH5 (residues 166–198), and aH6 (residues 217–246); and each c-subunit in the c_{12}-rotor ring (3–76). Also, it contains five segments of secondary structure that are not assigned to any specific subunit, defined as follows: chain V, residues 1,001–1,078 (probably either subunit b or b′); W, residues 1,001–1,124 (subunit b or b′); Y, residues 1,001–1,054 (two antiparallel transmembrane α-helices); 1, residues 1,001–1,020 (subunit δ or α_{DP}); 2, residues 1,001–1,015 (subunit δ or α_{DP} or b or b′); and 3, residues 1,001–1,019 (an α-helix parallel to the plane of the membrane). The structure also contains two additional α-helical segments containing residues 1–32 and 82–103 of the ζ-inhibitor. The nucleotide binding sites in the catalytic β_{DP}- and β_{TP}-subunits and the noncatalytic α_{TP}- and α_{DP}-subunits each contain ATP-Mg, and the nucleotide binding site in the α_E-subunit contains ADP-Mg. Neither substrates nor products are associated with the β_E-subunit.

Mode of Binding of the ζ-Inhibitor. The inhibitor is bound to the F_1 domain via residues 1–19 of the N-terminal α-helix, which occupy a cleft in the lower region of the $\alpha_{DP}\beta_{DP}$-catalytic interface (Fig. 2 *A* and *B*), with the rest of the α-helix (residues 20–32) extending from the surface of the enzyme. Residues 1 and 2 are close to residue Ser13 in the N-terminal α-helix of the γ-subunit, along the central axis of the F_1 domain. Residues 3–19 probably form polar and hydrophobic interactions with other residues in α-helices in the C-terminal domains of the α_{DP}- and β_{DP}-subunits (Fig. 2*C* and Table S2). α-Helix 4 (residues 82–103) is also resolved, stabilized by contacts with α-helix 1 and the α_{DP}-subunit (Table S3). In solution, residues 1–18 of the 107-aa chain of the ζ-inhibitor are unstructured, with the rest of the chain folded into a four-helix bundle (residues 19–42, 46–53, 66–77, and 81–103) (25). A complete fold of the ζ-inhibitor was constructed from the combined solution and crystal structures (Fig. 2*D*).

The N-terminal α-helix of the ζ-inhibitor protein is bound in a very similar way to how the inhibitory regions of bovine and yeast IF_1 bind to their cognate F_1-ATPases, and the structure of the

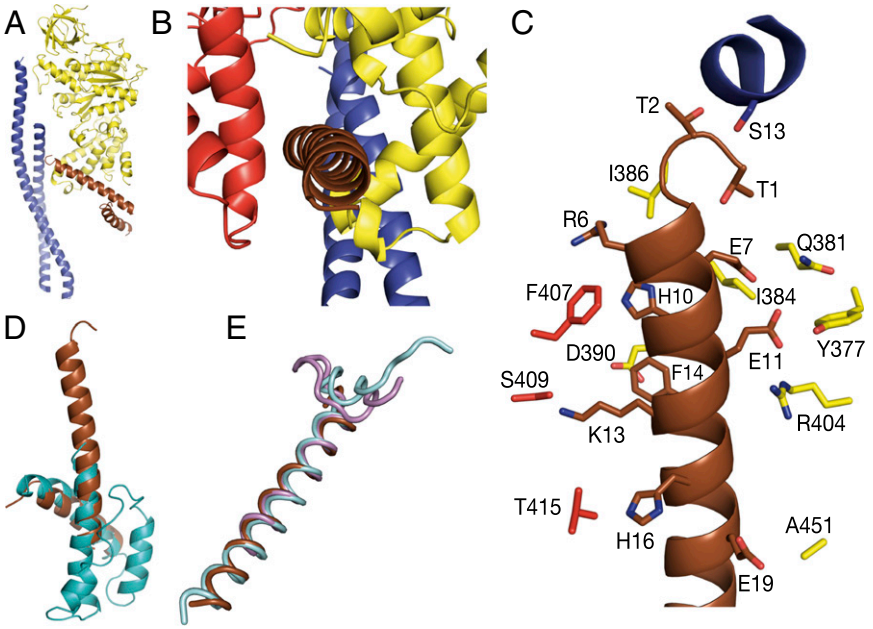

Fig. 2. Mode of binding of the ζ-inhibitor to the F-ATPase from *P. denitrificans*. The inhibitor is bound in the $\alpha_{DP}\beta_{DP}$-catalytic interface of the enzyme. (*A*) Cross-sectional side view of the F_1 domain showing the interaction of the ζ-inhibitor protein (brown) with the C-terminal domain of the β_{DP}-subunit (yellow) and the coiled-coil of α-helices in the γ-subunit (blue). (*B*) View from outside the complex toward the $\alpha_{DP}\beta_{DP}$-catalytic interface with the N-terminal α-helix of the ζ-inhibitor in a cleft between the α_{DP}- and β_{DP}-subunits. (*C*) Potential interactions between side chains of the ζ-inhibitor protein with residues in the α_{DP}-, β_{DP}-, and γ-subunits (Table S2). (*D*) Composite structure of the ζ-inhibitor by combination of residues 1–32 and 82–103 from the current study (brown) with residues 15–104 of the solution structure (cyan). (*E*) Superposition of the N-terminal region of the ζ-inhibitor (brown) with the corresponding inhibitory regions of IF_1 from bovine and yeast mitochondria (cyan and pink, respectively). The α-helical regions are residues 21–49, 16–36, and 3–24, respectively.

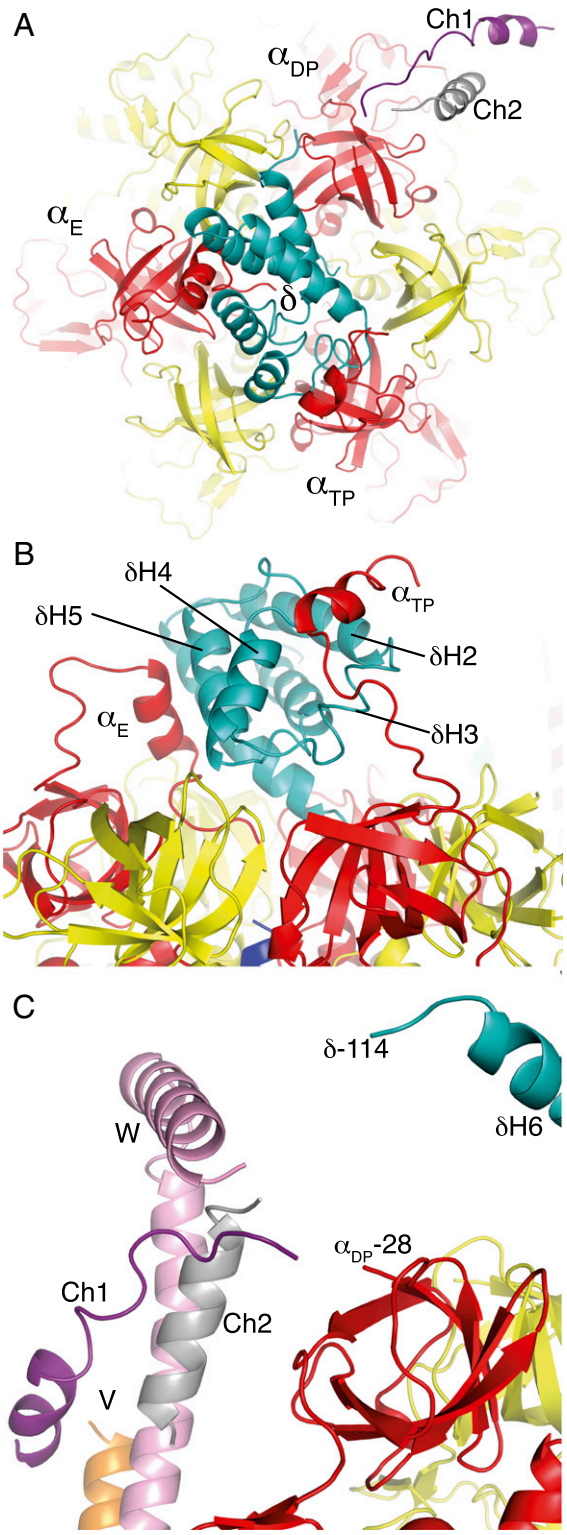

Fig. 3. Interactions of the δ-subunit with N-terminal regions of α-subunits in the F-ATPase from *P. denitrificans*. (*A*) View from above the F-ATPase toward the "crown" of the F_1 domain depicting the N-terminal regions of the α_E-, α_{TP}-, and α_{DP}-subunits (red) with the δ-subunit (blue), β-subunits (yellow) and chains 1 and 2 (Ch1 and Ch2; purple and gray, respectively). (*B*) Side view of the interactions of the α_E-subunit (residues 7–22) and the α_{TP}-subunit (residues 2–22) with helices δH1 and δH5 and helices δH2, δH3, and δH4, respectively. (*C*) Side view of the region around the N-terminal part of the α_{DP}-subunit with structural elements from peripheral stalk subunits.

bacterial F_1 domain resembles the bovine and yeast F_1-ATPases in their complexes with IF_1. The rmsd values for α-carbon superpositions of the *P. denitrificans* F_1 domain with the bovine and yeast F_1 domains in the inhibited complexes (3, 26) are 1.3 Å and 1.7 Å, respectively. The sequences of the inhibitory regions of the inhibitor proteins are also related weakly (Fig. S1), and their structures are very similar (Fig. 2*E*). All three inhibitors occupy equivalent positions in the $\alpha_{DP}\beta_{DP}$-catalytic interface, interacting with α-helices in the lower regions of their C-terminal domains.

The inhibitory regions of free bovine IF_1 and the free ζ-inhibitor are intrinsically disordered (4, 25), and the inhibitory region of yeast IF_1 is predicted to be so also (Table S4). It seems likely that the pathway of binding and folding of the inhibitory region of the ζ-inhibitor resembles the pathway of binding and folding of the inhibitory region of bovine IF_1, where the disordered inhibitory region interacts initially with the $\alpha_E\beta_E$-catalytic interface, the most open of the three catalytic interfaces, and closure of the interface is then driven by the hydrolysis of two ATP molecules first to the $\alpha_{TP}\beta_{TP}$-catalytic state and then to the $\alpha_{DP}\beta_{DP}$-catalytic state, accompanied by the progressive folding of the disordered region (4).

Connections with the Peripheral Stalk. The main interactions between the peripheral stalk and the F_1 domain of the enzyme involve the δ-subunit, which sits on top of the crown of the F_1 domain (Fig. 3*A*). The N-terminal domain of the *P. denitrificans* δ-subunit is folded into a bundle of six α-helices, as in the *E. coli* δ-subunit (20) and the orthologous bovine oligomycin sensitivity conferral protein subunit, OSCP (27, 28). The N-terminal regions of α-subunits project from the top of the crown, and α-helices in the N-terminal regions of the α_E- and α_{TP}-subunits (residues 2–22 and 7–22, respectively) interact with α-helices δH1 (residues 8–27) and δH5 (residues 79–91), and δH2 (residues 30–45), δH3 (residues 47–53), and δH4 (residues 61–68), respectively; only the first interaction was observed in the structure of the bovine F_1–peripheral stalk complex (28). The structure of the N-terminal region of the α_{DP}-subunit is unclear. It appears to be in a region of contiguity of structural elements from the N terminus of the α_{DP}-subunit and the C-terminal regions of the δ-, b-, and b′-subunits (Fig. 2*C*). Although they are not fully resolved in the current electron density map, this region involves the two unassigned element chains 1 and 2 that could be part of any one of the α_{DP}-, δ-, b-, or b′-subunits (Fig. 2*C*). It appears that this partially resolved region is mobile, and it may act as a hinge or elbow connecting to the well-defined, and probably rigid, α-helical region of the peripheral stalk. This region is composed of the approximately parallel α-helices in the b- and b′-subunits, but in the current map, these subunits cannot be distinguished with certainty. As in the structure of the bovine F_1–peripheral stalk complex, this extensive α-helical region is associated along the external surface of the noncatalytic $\alpha_{TP}\beta_{DP}$-interface, and so this conformation of the F-ATPase appears to represent an abundant, probably low-energy, state that allows the enzyme to crystallize from the many structural conformers of the F-ATPase complex. The α-helical region of the peripheral stalk extends almost to the membrane domain, where the electron density again becomes difficult to interpret, suggesting that this region may also be flexible.

Structure of the Membrane Domain. The resolved structure of the membrane domain of the F-ATPase from *P. denitrificans* (Figs. 1 and 4*A*) consists of a c_{12}-ring (gray); an associated bundle of four α-helices (green) with its axis tilted at about 30° to the plane of the membrane, with a fifth α-helix (magenta) sitting on top of the bundle close to the inner surface of the bacterial membrane; and two side-by-side α-helices (cyan) normal to the plane of the membrane. The c-ring is made of an inner ring of N-terminal α-helices and an outer ring of C-terminal α-helices, and the loops joining the helices make an extensive interface with the foot of the central stalk with a buried surface area of 522 $Å^2$. Together, the c-ring and the central stalk constitute the rotor of the enzyme.

BIOCHEMISTRY

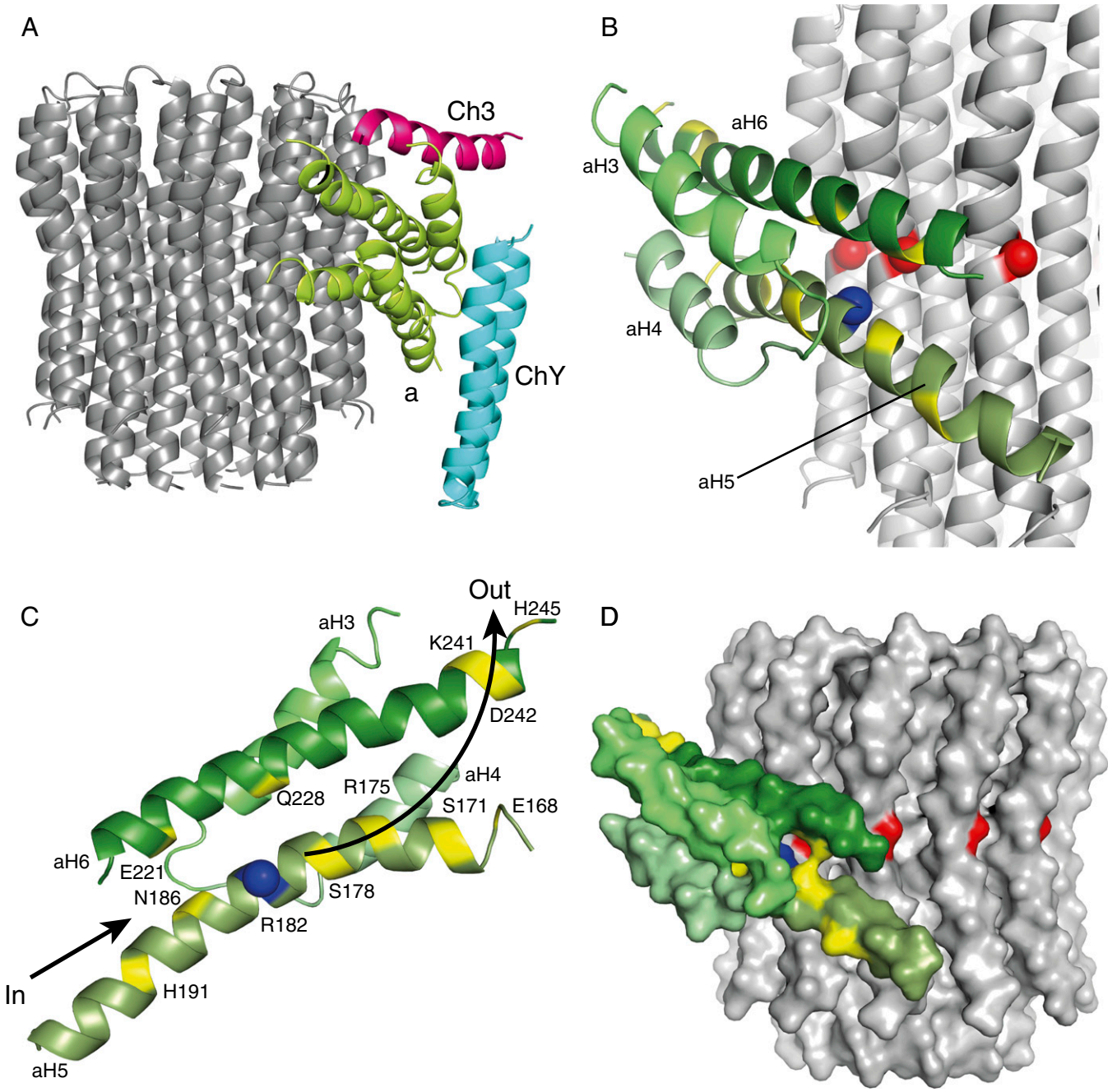

Fig. 4. Topography of the membrane domain of the F-ATPase from *P. dentrificans* and a potential pathway of transmembrane proton translocation. (*A*) View of the c_{12}-rotor ring, and an associated bundle of α-helices (green), assigned to the a-subunit and named aH3–aH4 (residues 1,001–1,035), and aH5 and aH6 containing residues 166–198 and 217–246, respectively (Figs. S2 and S3). Unassigned α-helix Ch3 and α-helical hairpin ChY are shown in magenta and blue, respectively. (*B*) View of the association of the tilted bundle of four α-helices in subunit a with the c-ring showing residue Glu60 (red) in the c-subunit in the proton transfer site and residue Arg182 (blue) in aH5. (*C*) View from the c-ring of the tilted bundle of four α-helices in subunit a showing conserved polar residues (yellow) that could provide the access path (In) for protons from the bacterial periplasm to reach the proton transfer site and the exit path (Out) for protons to be released into the bacterial cytoplasm. Residue Arg182 is colored blue. (*D*) View in solid representation of the tilted bundle of four α-helices in the a-subunit in juxtaposition with the c-ring showing the potential inlet pathway for protons (yellow) leading through the bundle to the proton transfer site containing a negatively charged Glu60 (red).

Based on the conservation of six hydrophobic segments in their sequences (Figs. S2 and S3), it is likely that the a-subunit has six transmembrane α-helices (aH1–aH6), whereas it has previously been considered to have five (corresponding to aH1–aH3, aH5, and aH6) (28). The four-helix bundle in the current structure has been attributed to α-helices aH3–aH6, where aH5 and aH6 consist of 29 and 32 residues, respectively, corresponding to the unusually long hydrophobic segments 5 and 6 in the sequences of a-subunits (Figs. S2 and S3). Segment 5 contains the absolutely conserved Arg residue Arg182, known from studies in *E. coli* to be essential for proton translocation through the membrane domain of the enzyme, and in the structure, as required, this residue is close to another essential residue Glu60 in the c-subunit (Fig. 4). Tilted α-helices aH3 and aH4 are shorter, as expected from the shorter hydrophobic sequence segments 3 and 4, and are packed close to aH5 and aH6. A tilted four-helix bundle has been observed also by cryo-EM,

nominally at 7 Å resolution, in the membrane domain of the F-ATPase from *Polytomella*, but aH5 and aH6 in *P. denitrificans* were assigned as aH6 and aH5, respectively, in *Polytomella* (29).

The high conservation of the sequences of a-subunits in the regions of aH5 and aH6 suggests that their structures will be conserved also (Fig. S3), and because there was no significant side-chain density, the sequence register assigned to these α-helices was based on biochemical data. The tilted transmembrane α-helix closer to the periplasm was identified as aH5 (containing the essential Arg182), because this interpretation agrees better with cross-linking experiments between the *E. coli* a- and c-subunits (30). However, the reported cross-link between *E. coli* residues 55 in subunit c and 207 in subunit a (residues 54 in subunit c and 179 in subunit a in *P. denitrificans*) does not fit with this model, but the yield of this cross-link was significantly lower (11–20%) than the remainder (20–40%). Additional cross-links involving residues in *E. coli* aH5 (residues 239–260) also suggest that residues in the upper part of cH2 are closer to *E. coli* aH5 (*P. denitrificans* aH6) (31). Moreover, the placement of aH5 is consistent with the demonstration that residues Ser206 and Asn214 in *E. coli* (Ser178 and Asn186 in *P. denitrificans*) are accessible from the cytoplasm and periplasm, respectively (32). Finally, the lower α-helix (Fig. 4) is significantly more curved (by 20°) than the upper α-helix, and it is in close contact with the c-ring over three adjacent c-subunits. This enhanced curvature is consistent with the assignment of aH5 as the lower helix because of the presence of a Pro residue at position 176 (conserved as Pro or Ala in many sequences), whereas there is no Pro in aH6 in *P. denitrificans* or in an appropriate region of aH5 in *E. coli* (the only Pro is at position 240). Crucially, this model of aH5 in the α-helical density places the essential Arg182 residue close to the essential carboxylate of Glu60 in the c-subunit. Moreover, it defines the position of the many polar residues N-terminal to Arg182, with their side chains occupying a narrow cleft between the a-subunit and the c-ring that leads to the cytoplasm (Fig. 4). In the *E. coli* enzyme, the activity of the second site suppressor mutant, Arg210Gln-Gln252Arg, in the a-subunit suggests that Gln252 is near to Arg210 (30). Therefore, *P. denitrificans* aH6 was modeled with the equivalent Gln228 close to Arg182 in aH5. Although there is strong electron density for both aH5 and aH6, it is relatively featureless (i.e., sausage-like), and because of the absence of either clear side-chain density or clear α-helical features for the polypeptide backbone, it is possible that this part of the model could be in error by as much as 3–4 Å. Therefore, side chains in this region have been truncated to the β-carbon atoms. It is not possible to assign residue numbers reliably to the α-helical hairpin region of the a-subunit based on the available data, and this poly-Ala chain has been given residue numbers 1,001–1,035.

Currently, neither α-helices aH1 and aH2 nor single anticipated membrane α-helices in the N-terminal regions of subunits b and b′ have been assigned (Fig. S2). Thus, the three remaining resolved hydrophobic segments in Ch3 and ChY (Fig. 4) could represent any of these unassigned α-helices. At the current level of detail, it is not possible to know whether the loop between aH3 and aH4 lies close to ChY or whether the loop (residues 199–216) between aH5 and aH6 extends to the periplasmic side of the membrane, as has been suggested in the *E. coli* protein (30).

Pathway of Transmembrane Proton Translocation. In current models to explain the generation of rotation of the c-ring, during ATP synthesis (33), protons from the bacterial periplasm access a negatively charged carboxylate of a Glu60 residue in the interface region between the c-ring and the a-subunit. Once neutralized, driven by the proton-motive force, the neutralized carboxyl makes a rotary substep by moving anticlockwise, as viewed from the cytoplasmic side of the ring, into the hydrophobic environment of the membrane. Neutralization of further negatively charged carboxylates brought successively into the proton transfer site in the interface region generates further rotary substeps. Following an almost complete rotation of the ring, each neutralized carboxyl reenters the interface between subunit a and the c-ring, and becomes reionized in a process mediated by the essential Arg182, releasing the protons through a second half-channel leading to the bacterial cytoplasm. A series of conserved polar residues in helices aH5 and aH6 could be part of a sloping entry half-channel leading through the a-subunit to the proton transfer site, and other conserved polar residues in the same region could be part of the exit half-channel (Fig. 4 *C* and *D*). Many of the human pathogenic mutations in the human a-subunit are located in residues in the proposed proton inlet pathway (34).

Perspectives. The current structure of the F-ATPase from *P. dentrificans* has provided new information about its mode of regulation by the ζ-inhibitor protein and about the association of the static a-subunit and the rotating c-ring, and the possible pathways by which the protons cross the membrane domain of the enzyme during the generation of rotation of the c-ring. To function, and for ATP synthesis to be coupled to the proton-motive force, the a-subunit has to be held in position against the rotating ring by being a component of the enzyme's stator (subunits a, b, b′, and δ, and the $\alpha_3\beta_3$-domain). Currently, crucial connections in the stator are unresolved, and the proton pathways lack the detail required for a full understanding of the coupling mechanism and the generation of rotation. Better diffracting crystals may provide a solution.

Materials and Methods

Protein Methods. The complex of the F-ATPase with the ζ-inhibitor was purified from cells of P. denitrificans and crystallized as described previously (24). These initial crystals diffracted X-rays to 6.8 Å resolution. Their diffraction properties were improved by seeding and by treatment of the resulting crystals with a solution of dicyclohexylcarbodiimide in DMSO, as follows. Crystals in a single well were broken into small fragments with a glass rod. The tip of a human hair was dipped into this suspension of microcrystals and drawn across the surface of a new well containing the F-ATPase and corresponding to the initial crystallization conditions. Crystals were grown at 25 °C for 10 d. Then, they were soaked for 8 h in a solution of dicyclohexylcarbodiimide in DMSO [final concentrations 5 mM and 1% (wt/vol)], respectively.

Data Collection and Structure Determination. Information on data collection and structure determination is provided in *SI Materials and Methods*.

ACKNOWLEDGMENTS. We thank Dr. T. B. Walpole for making the multiple sequence alignment of the a-subunit and the staff at Beamline I04-1 at the Diamond Light Source for their help. This work was funded by Medical Research Council (MRC) Intramural Program U105663150 and Program Grant MR/M009858/1 (to J.E.W.) and by MRC Intramural Program U105184325 (for A.G.W.L.). E.M.-R. was supported by an MRC Career Development Fellowship.

1. Watanabe R, Noji H (2013) Chemomechanical coupling mechanism of F_1-ATPase: catalysis and torque generation. *FEBS Lett* 587(8):1030–1035.
2. Walker JE (2013) The ATP synthase: The understood, the uncertain and the unknown. *Biochem Soc Trans* 41(1):1–16.
3. Robinson GC, et al. (2013) The structure of F_1-ATPase from *Saccharomyces cerevisiae* inhibited by its regulatory protein IF_1. *Open Biol* 3(2):120164.
4. Bason JV, Montgomery MG, Leslie AGW, Walker JE (2014) Pathway of binding of the intrinsically disordered mitochondrial inhibitor protein to F_1-ATPase. *Proc Natl Acad Sci USA* 111(31):11305–11310.
5. Bason JV, Montgomery MG, Leslie AGW, Walker JE (2015) How release of phosphate from mammalian F_1-ATPase generates a rotary substep. *Proc Natl Acad Sci USA* 112(19):6009–6014.
6. Baker LA, Watt IN, Runswick MJ, Walker JE, Rubinstein JL (2012) Arrangement of subunits in intact mammalian mitochondrial ATP synthase determined by cryo-EM. *Proc Natl Acad Sci USA* 109(29):11675–11680.
7. Foster DL, Fillingame RH (1979) Energy-transducing H^+-ATPase of *Escherichia coli*. Purification, reconstitution, and subunit composition. *J Biol Chem* 254(17):8230–8236.
8. Foster DL, Fillingame RH (1982) Stoichiometry of subunits in the H^+-ATPase complex of *Escherichia coli*. *J Biol Chem* 257(4):2009–2015.
9. Walker JE, Saraste M, Gay NJ (1984) The unc operon. Nucleotide sequence, regulation and structure of ATP-synthase. *Biochim Biophys Acta* 768(2):164–200.
10. Cingolani G, Duncan TM (2011) Structure of the ATP synthase catalytic complex (F_1) from *Escherichia coli* in an autoinhibited conformation. *Nat Struct Mol Biol* 18(6): 701–707.

11. Roy A, Hutcheon ML, Duncan TM, Cingolani G (2012) Improved crystallization of *Escherichia coli* ATP synthase catalytic complex (F_1) by introducing a phosphomimetic mutation in subunit ε. *Acta Crystallogr Sect F Struct Biol Cryst Commun* 68(Pt 10): 1229–1233.
12. Stocker A, Keis S, Vonck J, Cook GM, Dimroth P (2007) The structural basis for unidirectional rotation of thermoalkaliphilic F_1-ATPase. *Structure* 15(8):904–914.
13. Shirakihara Y, et al. (2015) Structure of a thermophilic F_1-ATPase inhibited by an ε-subunit: deeper insight into the ε-inhibition mechanism. *FEBS J* 282(15):2895–2913.
14. Shirakihara Y, et al. (1997) The crystal structure of the nucleotide-free $\alpha_3\beta_3$ subcomplex of F_1-ATPase from the thermophilic *Bacillus* PS3 is a symmetric trimer. *Structure* 5(6):825–836.
15. Meier T, Polzer P, Diederichs K, Welte W, Dimroth P (2005) Structure of the rotor ring of F-Type Na^+-ATPase from *Ilyobacter tartaricus*. *Science* 308(5722):659–662.
16. Pogoryelov D, Yildiz O, Faraldo-Gómez JD, Meier T (2009) High-resolution structure of the rotor ring of a proton-dependent ATP synthase. *Nat Struct Mol Biol* 16(10): 1068–1073.
17. Preiss L, et al. (2013) The c-ring stoichiometry of ATP synthase is adapted to cell physiological requirements of alkaliphilic *Bacillus pseudofirmus* OF4. *Proc Natl Acad Sci USA* 110(19):7874–7879.
18. Matthies D, et al. (2014) High-resolution structure and mechanism of an F/V-hybrid rotor ring in a Na^+-coupled ATP synthase. *Nat Commun* 5:5286.
19. Preiss L, et al. (2014) The c-ring ion binding site of the ATP synthase from *Bacillus pseudofirmus* OF4 is adapted to alkaliphilic lifestyle. *Mol Microbiol* 92(5):973–984.
20. Wilkens S, Borchardt D, Weber J, Senior AE (2005) Structural characterization of the interaction of the delta and alpha subunits of the Escherichia coli F1F0-ATP synthase by NMR spectroscopy. *Biochemistry* 44(35):11786–11794.
21. Dmitriev O, Jones PC, Jiang W, Fillingame RH (1999) Structure of the membrane domain of subunit b of the *Escherichia coli* F_oF_1 ATP synthase. *J Biol Chem* 274(22): 15598–15604.
22. Del Rizzo PA, Bi Y, Dunn SD, Shilton BH (2002) The "second stalk" of *Escherichia coli* ATP synthase: Structure of the isolated dimerization domain. *Biochemistry* 41(21): 6875–6884.
23. Priya R, Biukovic G, Gayen S, Vivekanandan S, Grüber G (2009) Solution structure, determined by nuclear magnetic resonance, of the b30-82 domain of subunit b of *Escherichia coli* F_1F_o ATP synthase. *J Bacteriol* 191(24):7538–7544.
24. Morales-Ríos E, et al. (2015) Purification, characterization and crystallization of the F-ATPase from *Paracoccus denitrificans*. *Open Biol*, 10.1098/rsob.150119.
25. Serrano P, Geralt M, Mohanty B, Wüthrich K (2014) NMR structures of α-proteobacterial ATPase-regulating ζ-subunits. *J Mol Biol* 426(14):2547–2553.
26. Gledhill JR, Montgomery MG, Leslie AGW, Walker JE (2007) How the regulatory protein, IF_1, inhibits F_1-ATPase from bovine mitochondria. *Proc Natl Acad Sci USA* 104(40):15671–15676.
27. Carbajo RJ, et al. (2007) How the N-terminal domain of the OSCP subunit of bovine F_1F_o-ATP synthase interacts with the N-terminal region of an alpha subunit. *J Mol Biol* 368(2):310–318.
28. Rees DM, Leslie AGW, Walker JE (2009) The structure of the membrane extrinsic region of bovine ATP synthase. *Proc Natl Acad Sci USA* 106(51):21597–21601.
29. Allegretti M, et al. (2015) Horizontal membrane-intrinsic α-helices in the stator a-subunit of an F-type ATP synthase. *Nature* 521(7551):237–240.
30. Fillingame RH, Steed PR (2014) Half channels mediating H^+ transport and the mechanism of gating in the F_o sector of *Escherichia coli* F_1F_o ATP synthase. *Biochim Biophys Acta* 1837(7):1063–1068.
31. Moore KJ, Fillingame RH (2008) Structural interactions between transmembrane helices 4 and 5 of subunit a and the subunit c ring of *Escherichia coli* ATP synthase. *J Biol Chem* 283(46):31726–31735.
32. Dong H, Fillingame RH (2010) Chemical reactivities of cysteine substitutions in subunit a of ATP synthase define residues gating H^+ transport from each side of the membrane. *J Biol Chem* 285(51):39811–39818.
33. Junge W, Nelson N (2015) ATP synthase. *Annu Rev Biochem* 84:631–657.
34. Xu T, Pagadala V, Mueller DM (2015) Understanding structure, function, and mutations in the mitochondrial ATP synthase. *Microb Cell* 2(4):105–125.
35. Winn MD, et al. (2011) Overview of the CCP4 suite and current developments. *Acta Crystallogr D Biol Crystallogr* 67(Pt 4):235–242.
36. Battye TG, Kontogiannis L, Johnson O, Powell HR, Leslie AGW (2011) iMOSFLM: A new graphical interface for diffraction-image processing with MOSFLM. *Acta Crystallogr D Biol Crystallogr* 67(Pt 4):271–281.
37. Evans PR, Murshudov GN (2013) How good are my data and what is the resolution? *Acta Crystallogr D Biol Crystallogr* 69(Pt 7):1204–1214.
38. McCoy AJ, et al. (2007) Phaser crystallographic software. *J Appl Crystallogr* 40(Pt 4): 658–674.
39. Morales-Ríos E, Montgomery MG, Leslie AGW, Walker JE (2015) Structure of a catalytic dimer of the α- and β-subunits of the F-ATPase from *Paracoccus denitrificans* at 2.3 Å resolution. *Acta Cryst*, 10.1107/S2053230X15016076.
40. Emsley P, Lohkamp B, Scott WG, Cowtan K (2010) Features and development of Coot. *Acta Crystallogr D Biol Crystallogr* 66(Pt 4):486–501.
41. Gibbons C, Montgomery MG, Leslie AG, Walker JE (2000) The structure of the central stalk in bovine $F(_1)$-ATPase at 2.4 A resolution. *Nat Struct Biol* 7(11):1055–1061.
42. Rodgers AJ, Wilce MC (2000) Structure of the gamma-epsilon complex of ATP synthase. *Nat Struct Biol* 7(11):1051–1054.
43. Murshudov GN, et al. (2011) REFMAC5 for the refinement of macromolecular crystal structures. *Acta Crystallogr D Biol Crystallogr* 67(Pt 4):355–367.
44. Nicholls RA, Fischer M, McNicholas S, Murshudov GN (2014) Conformation-independent structural comparison of macromolecules with ProSMART. *Acta Crystallogr D Biol Crystallogr* 70(Pt 9):2487–2499.
45. Chen VB, et al. (2010) MolProbity: All-atom structure validation for macromolecular crystallography. *Acta Crystallogr D Biol Crystallogr* 66(Pt 1):12–21.
46. Li X, Romero P, Rani M, Dunker AK, Obradovic Z (1999) Predicting Protein Disorder for N-, C-, and Internal Regions. *Genome Inform Ser Workshop Genome Inform* 10:30–40.
47. Linding R, et al. (2003) Protein disorder prediction: Implications for structural proteomics. *Structure* 11(11):1453–1459.
48. Krissinel E, Henrick K (2007) Inference of macromolecular assemblies from crystalline state. *J Mol Biol* 372(3):774–797.
49. Krogh A, Larsson B, von Heijne G, Sonnhammer EL (2001) Predicting transmembrane protein topology with a hidden Markov model: Application to complete genomes. *J Mol Biol* 305(3):567–580.